ÉCOLE POLYTECHNIQUE FÉDÉRALE DE LAUSANNE

MATHICSE

Mathematics Institute of Computational Science and Engineering

School of Basic Sciences - Section of Mathematics

MATHICSE Technical Report

Nr. 06.2016

February 2016

Computational comparison of aortic root stresses in presence of stentless and stented aortic valve bio-prostheses

M.G.C. Nestola, E. Faggiano, C. Vergara, R.M. Lancellotti,
S. Ippolito, S. Filippi, A. Quarteroni, R. Scrofani

http://mathicse.epfl.ch

Phone: +41 21 69 37648

Address:
EPFL - SB - MATHICSE (Bâtiment MA)
Station 8 - CH-1015 - Lausanne - Switzerland

Fax: +41 21 69 32545

Submitted to *Computer Methods in Biomechanics and Biomedical Engineering*
Vol. 00, No. 00, Month 20XX, 1–14

Computational comparison of aortic root stresses in presence of stentless and stented aortic valve bio-prostheses

M.G.C. Nestola[a], E. Faggiano[b,c], C. Vergara[d], R.M. Lancellotti[e], S.Ippolito [f], S. Filippi[g,h], A. Quarteroni[i], and R. Scrofani[l]

[a]Institute of Computational Science (ICS), Faculty of Informatics, University of Lugano Via Buffi 13, 6904 Lugano, +41 58 666 4455, nestom@usi.ch
[b]MOX, Dipartimento di Matematica, Politecnico di Milano, Piazza Leonardo da Vinci 32, 20133, Milan, Italy, +39 0223994699, elena.faggiano@gmail.com
[c]Labs, Department of Chemistry, Materials and Chemical Engineering "Giulio Natta", Politecnico di Milano, Piazza Leonardo da Vinci 32, 20133, Milan, Italy
[d]MOX, Dipartimento di Matematica, Politecnico di Milano, Piazza Leonardo da Vinci 32, 20133, Milan, Italy, +39 0223994610, christian.vergara@polimi.it
[e]MOX, Dipartimento di Matematica, Politecnico di Milano, Piazza Leonardo da Vinci 32, 20133, Milan, Italy, +39 0223994604, roccomichele.lancellotti@polimi.it
[f]Divisione di Radiologia, Ospedale L.Sacco, Via G.B. Grassi, 74 20157 Milan, Italy, +39 0239041, ippolito.sonia@hsacco.it
[g]International Center for Relativistic Astrophysics Network - I.C.R.A.Net
[h]Nonlinear Physics and Mathematical Modeling Lab., Dipartimento di Ingegneria, Università Campus Bio-Medico di Roma, Italy, +39 06.22541.9611, S.Filippi@unicampus.it
[i]SB MATHICSE CMCS, EPFL, Av. Piccard, Bat. MA, Sec. B2-C2, Station 8, CH-1015 Lausanne, Switzerland, +41 (21) 693 2555, alfio.quarteroni@epfl.ch
[l]Divisione di Cardio-Chirurgia, Ospedale L.Sacco, Via G.B. Grassi, 74 20157 Milan, Italy, +39 0239041, scrofani.roberto@hsacco.it

(*Received 00 Month 20XX; accepted 00 Month 20XX*)

We provide a computational comparison of the performance of stentless and stented aortic prostheses, in terms of aortic root displacements and internal stresses. To this aim, we consider three real patients; for each of them we draw the two prostheses configurations, which are characterized by different mechanical properties. Moreover, for each patient, we consider also the native configuration. For each scenario, we solve the fluid-structure interaction problem arising between blood and aortic root, through Finite Elements. The results show a better agreement between stentless and native displacements and stresses, with respect to the stented case.

Keywords: Stentless aortic prosthesis, fluid-structure interaction, geometry deflation, Finite Elements Analysis

1. Introduction

Aortic valve pathologies represent an important cause of morbidity and mortality in industrialized countries (Lloyd-Jones, Adams, et al. 2010). The two main pathologies affecting the performance of the aortic valve are the *stenosis* and the *insufficiency*. A native valve affected by one of these pathologies requires a surgical treatment in order to restore its physiological performance. The most

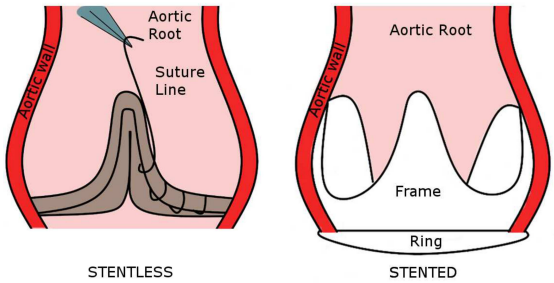

Figure 1. Simplified representation of the stentless (left) and stented (right) biological prostheses.

common surgical treatment consists in the valve replacement through mechanical or biological tissue valves. In principle, the new implanted aortic valve should provide wall stresses pattern similar to the native one.

The classical biological prosthesis used to replace the aortic valve is the *stented* one, consisting of porcine aortic valve or bovine pericardium leaflets mounted on a polymeric frame (the stent) surrounded by a synthetic sewing ring. The stented prosthesis is implanted by suturing the synthetic ring to the aortic annulus (see Figure 1, right). More recently, a new type of bio-prosthesis has been considered, namely the *stentless* one. This is obtained from the stented prosthesis by eliminating the valvular sewing ring and the stent rigid support. This prosthesis requires a minimal invasive implantation procedure with a single suture line running around the three sinuses of Valsalva (Beholz, Claus, et al. 2006), see Figure 1, left. Clinical investigations comparing stented and stentless prostheses showed that the latter improves hemodynamic parameters in terms of pressure gradient, valve orifice area, and ventricle mass regression (Beholz, Claus, et al. 2006; Dunning, Graham, et al. 2007).

In this contest, computational analyses based on the Finite Element Method may greatly contribute to investigate the performance of the biological prostheses, in terms of a quantification of stresses induced within the aortic root (Cacciola, Peters and Schreurs 2000; Xiong, Goetz, et al. 2010; Arcidiacono, Corvi and Severi 2005; Smuts, Blaine, et al. 2011; Auricchio, Conti, et al. 2011, 2014; Morganti, Conti, et al. 2014; De Hart, Peters, et al. 2003, 2004; De Hart, Baaijens, et al. 2003; Hsu, Kamensky, et al. 2014; Kamensky, Hsu, et al. 2014). The aim of this work is to compare the performance of stentless and stented prostheses in terms of mechanical stresses induced within the aortic root wall by the blood. To do this, we performed a computational study based on wall-blood FSI simulations in real geometries. For each geometry, we drew the stented, the stentless, and the native configurations. The characterization of the three scenarios was based on a different choice of the structural properties of the aortic root, to account for the frame in the stented case and for the suture in the stentless one.

2. Material and methods

2.1 *Patient dataset*

Our dataset comprised three patients routinely referred to the Cardiac-Surgery Department of Ospedale Sacco, Milan, Italy. Patients 1 and 2 featured a tricuspid aortic valve, whereas Patient 3 a bicuspid one. All the patients suffered from a calcific aortic valve stenosis confirmed by the elevated values of the transvalvular pressure gradient, see Table 1. Accordingly, they were subjected to a surgical treatment consisting in aortic valve replacement with the Freedom Sorin SOLO stentless biological prosthesis. Other details about the three patients can be found in Table 1.

A Philips Brilliance CT 64-slice system was employed to perform a post-surgery three dimensional Contrast Enhanced Computed Tomography (3D-CE-CT) study with a slice thickness of $0.67\,mm$,

	Age	Sex	Pre-operative TPG (mmHg)	Average aortic root thickness (mm)	Inlet area (cm^2)
Patient 1	33	M	68	2.6	3.02
Patient 2	65	M	52	2.1	3.68
Patient 3	84	M	44	2.5	3.92

Table 1. Data related to the three patients considered in the present study. TPG=tranvalvular pressure gradient.

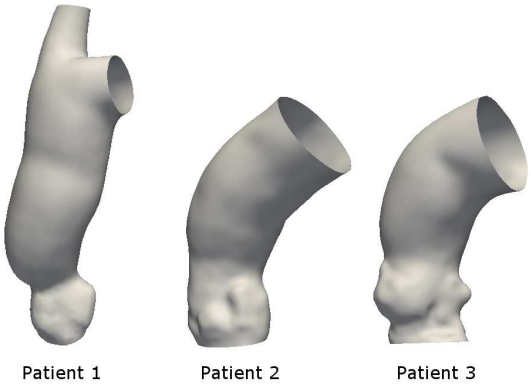

Figure 2. Lumen boundary surfaces reconstructed from CT images.

a slice spacing of $0.33mm$, a reconstruction matrix of 512 $\times$512 pixels, and a final resolution of $0.45mm \times 0.45mm \times 0.33mm$. 3D-CE-CT images were acquired at different instants of the cardiac cycle. A CE-CT slice 3.74 mm thick was positioned in the plane of the valve in order to acquire a valvular in-plane image. International Review Broad approval was obtained for the conduct of this study, and the board waived the need for patient consent.

2.2 *Geometry reconstruction and mesh generation*

To perform the reconstructions of the aortic geometries we started from the 3D-CE-CT scans corresponding to the diastolic phase. A surface model of the aortic root and ascending aorta was obtained for each patient using a level set-segmentation technique implemented in the Vascular Modeling Toolkit (vmtk, www.vmtk.org) (Antiga, Piccinelli, et al. 2008), see Figure 2. The internal volume of this surface, occupied by the fluid, was then discretized using tetrahedral mesh as in Faggiano and Antiga (in preparation). Moreover, a solid grid was obtained by extrusion, with four layers of tetrahedra generated from the interface surface with a total wall thickness equal to 20% of the local vessel radius. This allowed to obtain average values of the wall thickness (see Table 1) which are compatible with the ranges reported in the literature (see, e.g., Summers, Andrasko-Bourgeois, et al. (1998)). Finally, we performed a mesh refinement of the fluid and wall meshes in the region of the aortic root (see Figure 3, left). For each of the three patients, the final number of tetrahedra was about 3×10^5 for the fluid domain and about 1.9×10^5 for the solid domain. This mesh size was determined once the peak of the *Von Mises stresses* did not change by more than 4% between successive refinements.

2.3 *Characterization of the different scenarios*

For each patient we virtually designed the regions of the prostheses in contact with the aortic root (the frame for the stented case and the suture for the stentless case), and we selected different mechanical behavior in these regions with respect to the native wall. For any case, we assigned two of the four wall layers to the biological prosthesis and the remaining two to the aortic wall (see Figure 3, right). This choice was motivated by the fact that a stented prosthesis has commonly a

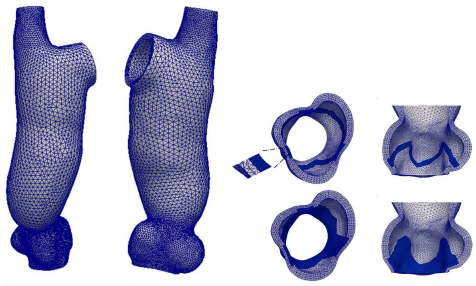

Figure 3. On the left: Fluid mesh (left) and structure mesh (right). On the right: Aortic root in the stentless (up) and stented (bottom) configurations. In blue we depicted the regions characterized by different mechanical properties with respect to the native configuration. Patient 1.

thickness in the range $(0.5, 1.5)\,mm$ (Angell and Yoon 1977). Then, considering the average aortic root thickness reported in Table 1, we found that our choice lead to a stented prosthesis thickness falling in the reported range. Similar considerations hold for the stentless case.

Stented prosthesis
The stented prosthesis is composed of three elements (see Figure 1, right):

(1) a flexible frame used as a skeleton and covered with a biocompatible material;
(2) a base ring used to suture the prosthesis to the aortic annulus during the implantation;
(3) the leaflets, made of bovine pericardium or obtained by using porcine aortic valve.

We decided to model the flexible frame and the base ring as a homogeneous and isotropic structure inside the aortic root, see Figure 3, right-bottom.

Stentless prosthesis
In this case the valve is sutured directly to the aortic root without any frame, see Figure 1, left. Thus, we modeled the suture strip running around the three sinuses of Valsalva as a homogeneous and isotropic structure inside the aortic root, see Figure 3, right-up. To obtain a realistic configuration of the suture, we reproduced its pattern with the help of an expert clinician, looking at the 3D-CE-CT image of the patient.

Native aortic valve
In view of a complete comparison, we also considered for each patient the scenario representing the native case, obtained by considering constant-in-space parameters in all the aortic root.

We point out that in all the cases the modelling of the leaflets was neglected. The choice of representing the three scenarios (stentless, stented, native) in the same geometry was aimed at isolating the effect of the different biological prostheses, leaving unchanged all the other sources of perturbation (geometry, boundary conditions, etc).

2.4 *Governing equations and numerical solution*

Referring to Figure 4, left, let Ω_f be the current fluid domain. We considered the Navier-Stokes equations for an incompressible, homogeneous, Newtonian fluid, written in the *Arbitrary Lagrangian-Eulerian* (ALE) configuration (Hughes, Liu and Zimmermann 1981).

Let Ω_s be the current structural domain, see Figure 4, right. We considered an elastic material and the unsteady elasto-dynamic problem written in the Lagrangian configuration.

For any function g defined in the current fluid (solid) configuration, we denoted by $\widehat{g}$ its counterpart in the reference domain $\widehat{\Omega}_f$ ($\widehat{\Omega}_s$). The common current fluid-structure interface has been denoted by Σ. Then, the differential formulation of the FSI problem reads as follows:

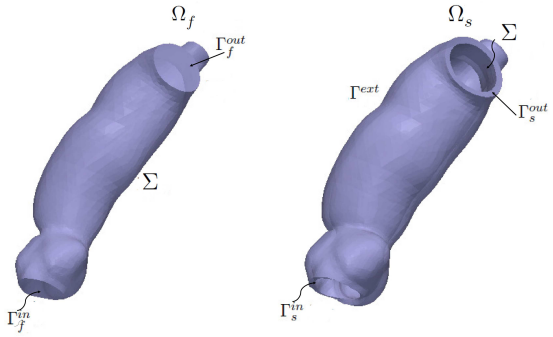

Figure 4. Computational domains. Fluid domain on the left, structure domain on the right.

Find, at each time $t \in (0, T]$, fluid velocity $\boldsymbol{u}_f$, pressure p_f, structure displacement $\boldsymbol{\eta}_s$ and fluid domain displacement $\boldsymbol{\eta}_m$, such that

$$-\triangle\widehat{\boldsymbol{\eta}}_m = \boldsymbol{0} \qquad \text{in } \widehat{\Omega}_f, \tag{1a}$$

$$\widehat{\boldsymbol{\eta}}_m = \widehat{\boldsymbol{\eta}}_s \qquad \text{at } \widehat{\Sigma}, \tag{1b}$$

$$\rho_f \frac{D^A \boldsymbol{u}_f}{Dt} + \rho_f((\boldsymbol{u}_f - \boldsymbol{u}_m)\cdot\nabla)\boldsymbol{u}_f - \nabla\cdot\boldsymbol{T}_f = \boldsymbol{0} \qquad \text{in } \Omega_f, \tag{1c}$$

$$\nabla\cdot\boldsymbol{u}_f = 0 \qquad \text{in } \Omega_f, \tag{1d}$$

$$\boldsymbol{u}_f = \boldsymbol{g} \qquad \text{at } \Gamma_f^{in}, \tag{1e}$$

$$\frac{1}{|\Gamma_f^{out}|}\int_{\Gamma_f^{out}} (\boldsymbol{T}_f\,\boldsymbol{n})\cdot\boldsymbol{n}\,d\sigma - R_e\int_{\Gamma_f^{out}} \boldsymbol{u}_f\cdot\boldsymbol{n}\,d\sigma = P^{out} \qquad \text{at } \Gamma_f^{out}, \tag{1f}$$

$$\boldsymbol{u}_f = \frac{\partial\boldsymbol{\eta}_s}{\partial t} \qquad \text{at } \Sigma, \tag{1g}$$

$$\boldsymbol{T}_s(\boldsymbol{\eta}_s)\,\boldsymbol{n} - \boldsymbol{T}_f(\boldsymbol{u}_f, p_f)\,\boldsymbol{n} = \boldsymbol{0} \qquad \text{at } \Sigma, \tag{1h}$$

$$\rho_s\frac{\partial^2\widehat{\boldsymbol{\eta}}_s}{\partial t^2} - \nabla\cdot\widehat{\boldsymbol{T}}_s(\widehat{\boldsymbol{\eta}}_s) = \boldsymbol{0} \qquad \text{in } \widehat{\Omega}_s, \tag{1i}$$

$$\widehat{\boldsymbol{\eta}}_s = \boldsymbol{0} \qquad \text{at } \Gamma_s, \tag{1j}$$

$$\alpha_e\widehat{\boldsymbol{\eta}}_s + \widehat{\boldsymbol{T}}_s(\widehat{\boldsymbol{\eta}}_s)\,\widehat{\boldsymbol{n}} = \boldsymbol{0}, \qquad \text{at } \widehat{\Gamma}^{ext}, \tag{1k}$$

where $\Gamma_s = \Gamma_s^{in} \cup \Gamma_s^{out}$, $\widehat{\boldsymbol{u}}_m := \frac{\partial\widehat{\boldsymbol{\eta}}_m}{\partial t}$ is the fluid mesh velocity.

In the previous coupled problem, (1a) represents the harmonic extension for the computation of the fluid domain, (1c)-(1f) the fluid problem, and (1i)-(1k) the structure problem. Moreover, μ is the constant blood viscosity, ρ_f and ρ_s the fluid and structure densities, $\boldsymbol{n}$ the unit normal exiting from the structure domain, $\frac{D^A}{Dt}$ the ALE derivative, $\boldsymbol{T}_f(\boldsymbol{u}_f, p_f) = \mu\left(\nabla\boldsymbol{u}_f + (\nabla\boldsymbol{u}_f)^T\right) - p\,\boldsymbol{I}$ the fluid Cauchy stress tensor, whereas $\widehat{\boldsymbol{T}}_s(\widehat{\boldsymbol{\eta}}_s)$ is the first Piola-Kirchhoff tensor and $\boldsymbol{T}_s(\boldsymbol{\eta}_s)$ the Cauchy stress tensors of the solid. In this work we used a nearly incompressible *exponential* material (Demiray 1972), characterized by the following strain energy function

$$W = \frac{\kappa}{4}[(J-1)^2 + (\log J)^2] + \frac{G}{2\gamma}\left(\exp\{\gamma(\mathrm{tr}(\bar{\boldsymbol{C}}) - 3)\} - 1\right), \tag{2}$$

where $\bar{\boldsymbol{C}} = J^{-\frac{2}{3}}\boldsymbol{F}^T\boldsymbol{F}$, $\boldsymbol{F} = \nabla_{\widehat{\boldsymbol{x}}_s}\boldsymbol{x}_s$, $J = det(\boldsymbol{F})$, κ is the *bulk modulus* and G the *shear modulus*. For small deformations this material behaves as a linear structure where the Poisson's ratio ν and

the Young modulus E are related to κ and G as follows

$$\kappa = \frac{E}{3(1-2\nu)}, \qquad G = \frac{E}{2(1+\nu)}. \tag{3}$$

The parameter γ characterizes the stiffness of the material for large displacements. The exponential law to describe the aortic wall allows to account for the elastic behavior at very small displacements and for the strong stiffening due to collagen fibers for higher deformations (Holzapfel and Ogden 2010). It has been successfully used to describe the aortic vessel in García-Herrera and Celentano (2013). Moreover, P^{out} is the external pressure and R_e is the resistance used to enforce absorbing boundary conditions at the fluid outlets, see Nobile, Pozzoli and Vergara (2013). At the lateral structure surface Γ^{ext}, we prescribed the Robin condition (1k) to account for the elastic behavior of the surrounding tissue, characterized by the elastic parameter α_e (Moireau, Xiao, et al. 2012).

At the FS interface, we wrote the matching conditions, which state the continuity of velocities (1g) and the continuity of tractions (1h) (*physical interface conditions*), whereas condition (1b) enforces the continuity of displacements (*geometrical interface condition*).

Finally, we observe that problem (1) has to be endowed with suitable initial conditions.

For the numerical solution of problem (1), after the time discretization, we considered at each time step the partitioned algorithm proposed in Nobile, Pozzoli and Vergara (2014) where the geometrical coupling and the constitutive non-linearities are tretaed inexactly, whereas the physical coupling conditions are enforced exactly by using the *Robin-Robin* (RR) scheme proposed in Badia, Nobile and Vergara (2008). This inexact scheme is accurate and stable for hemodynamic applications, see Nobile, Pozzoli and Vergara (2014).

2.5 *Including the diastolic pressure*

In this work we considered a non-linear elastic material, so that we could not ignore the non-null diastolic blood pressure characterizing the radiological images used for the geometry reconstructions. To appropriately account for the blood pressure inside the diastolic geometry, one could introduce a pre-stress in the first Piola-Kirchhoff stress tensor (Hsu and Bazilevs 2011), consider a modified updated Lagrangian formulation (Gee, Reeps, et al. 2009), or solve a backward elastodynamic problem (de Putter, Wolters, et al. 2007; Lu, Zhou and Raghavan 2007). Here, we used the strategy introduced in Lancellotti (2012) and Bols, Degroote, et al. (2013). In particular, the idea is to recover through the introduction of an inverse problem, the *zero-stress* geometry (that is the one one would have without the blood inside the lumen) by suitably deflating the diastolic one. This inverse problem has been solved introducing fixed point iterations (see Lancellotti (2012) for more details).

2.6 *Generalities of the numerical simulations*

The values of the parameters involved in (2) are collected in Table 2. For the choice of parameters E and ν we referred to the values reported in Koch, Reddy, et al. (2010) for the nativey aortic wall, in Arcidiacono, Corvi and Severi (2005) for the bovine pericardium prosthesis, and in Bernacca, OConnor, et al. (2002); Mackay, Wheatley, et al. (1996); Grande-Allen, Cochran, et al. (2001); Wheatley, Fisher and Williams (2001) for the rigid frame in the stented prosthesis. The corresponding values of the shear modulus G and of the bulk modulus κ were then computed by using equation (3). In addition, the value of γ was set in agreement with Horgan and Saccomandi (2003).

The material density ρ_s was assumed to be constant in each solid sub-domain and equal to $1.1\, g\, cm^{-3}$ (see Grande-Allen, Cochran, et al. (2001), where a polimeric graft with the same density of the native wall has been studied, and De Hart, Baaijens, et al. (2003), where it has been

	G	κ	γ	E	ν
native vessel	0.34	16.67	1	1	0.49
bovine pericardial sheet	1.34	66.67	1	4	0.49
rigid frame	3.70	11.11	1	10	0.35

Table 2. Values of material parameters adopted for the the numerical simulations. G, κ and E are measured in MPa.

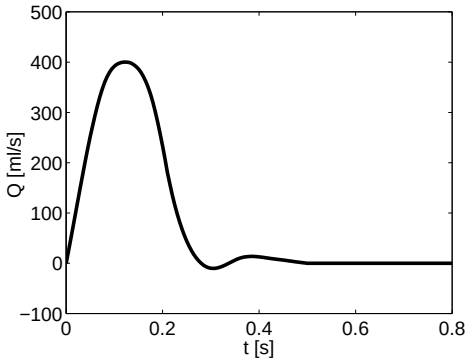

Figure 5. Flow rate used to prescribe the velocity profile at the inlet of the fluid domain.

highlighted that the bovine pericardium has a density comparable with the one of the human aorta), as well as the fluid density $\rho_f = 1.0\, g\, cm^{-3}$ and the dynamic viscosity $\mu = 0.035\, poise$. We also set in condition (1k) $\alpha_e = 500000\, dyne\, cm^{-3}$ (Moireau, Xiao, et al. 2012) and $P^{out} = 80\, mmHg$ in condition (1f). These choices allowed to recover a pressure in the physiological range $(80 - 120\, mmHg)$.

For each of the three scenarios, at the inlet Γ_{in}^f of the fluid domain we prescribed a flat velocity profile (Moireau, Xiao, et al. 2012) obtained at each time step by dividing the pulsatile flow rate shown in Figure 5 (Nordmeyer, Riesenkampff, et al. 2013; Olufsen, Peskin, et al. 2000) by the inlet section area. The values of the latter, reported in Table 1, featured similar values, so that we prescribed comparable velocities at the inlet. The unsteady numerical simulations were performed along the entire heart beat by using the parallel Finite Element Library LIFEV (www.lifeV.org). We used P1-P1 finite elements stabilized with the Interior Penalty technique (Burman and Hansbo 2006) for the fluid problem and P1 finite elements for the structure problem. We adopted the BDF1 scheme for the time integration of both the fluid and structure subproblems with a time step equal to $0.001\, s$.

3. Results

Although we ran our simulations for all the heartbeat, we performed our analysis only at the systolic peak, when the valve is completely open, the fluid jet achieved its maximum strength, and its influence on the arterial vessel is higher in terms of deformations and stresses.

3.1 *Blood flow dynamics in the aortic root*

The systolic blood streamlines in the three patients for the stentless case are shown in Figure 6. One may observe a fully developed jet with a maximum velocity of about $180\, cm\, s^{-1}$ formed downstream the aortic orifice, which remained confined to the core region of the aortic root. Similar patterns were also found in the native and stented cases (not shown).

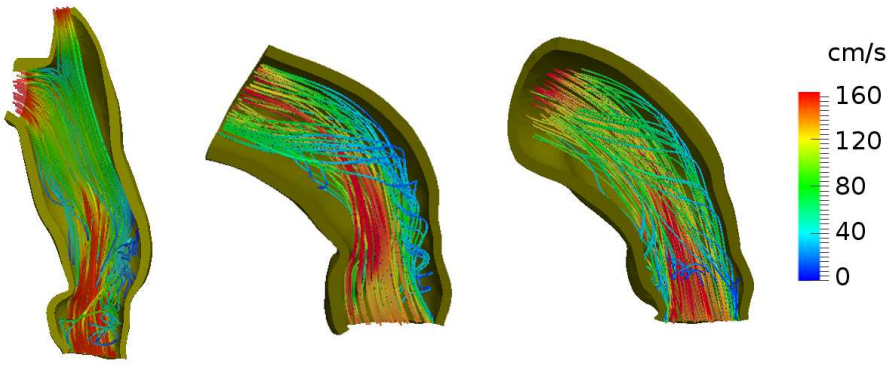

Figure 6. Peak systolic streamlines of the velocity field in the stentless case. Patient 1 (left), Patient 2 (middle), and Patient 3 (right).

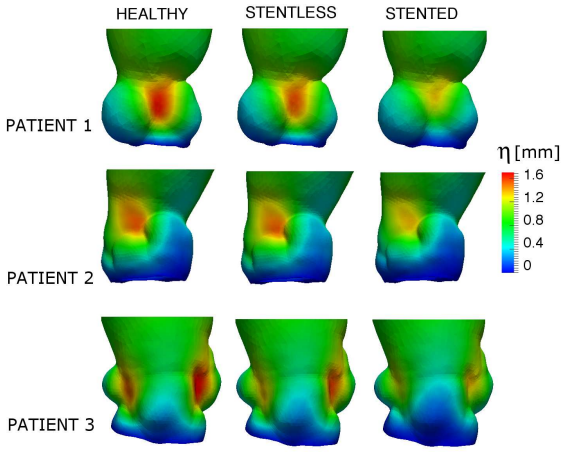

Figure 7. Spatial distribution at peak systole of the magnitude of the displacement field, η, in the aortic root of Patient 1, Patient 2 and Patient 3, respectively.

3.2 *Mechanical analysis of the aortic root*

The aim was to compare the mechanical performance of the stentless and stented bio-prostheses with the one featured by the native case.

3.2.1 Analysis of the aortic root displacements

Figure 7 shows the spatial distribution of the magnitude of the systolic displacement field $\eta(\boldsymbol{x}) = \|\boldsymbol{\eta}_s(t_s, \boldsymbol{x})\|_{\mathbb{R}^3}$. One may note that the stentless prosthesis allowed the aortic root to recover the native displacements, whereas the presence of the rigid frame in the stented one prevented the physiological dilation of the aortic root. To be more precise, referring to the volumes of interest reported in Figure 8, in Table 3 we reported the values of the average systolic displacement $\eta_s^{AV} = \|\boldsymbol{\eta}_s^{AV}\|_{\mathbb{R}^3}$, where $\eta_{s,i}^{AV} = \frac{1}{|\mathcal{V}|}\int_{\mathcal{V}} \eta_{s,i}(t_s, \boldsymbol{x})d\boldsymbol{x}$, and of the maximum in space systolic displacement $\eta_s^{MAX} = \max_{\boldsymbol{x}\in\mathcal{V}} \|\boldsymbol{\eta}_s(t_s, \boldsymbol{x})\|_{\mathbb{R}^3}$, t_s being the systolic instant. These results confirmed the qualitative analysis suggested by Figure 7. Indeed, negligible differences were found between the values assumed in the stentless and native scenarios, whereas significant variations were found in the stented configuration. In particular, in this case the values of η_s^{AV} and η_s^{MAX} were about 20% lower than those computed in the physiological condition.

Figure 8. Representation of the volumes of interest $\mathcal{V}$ (in red) for Patient 1 (left), Patient 2 (middle), Patient 3 (right). Here L and R refer to the left-coronary and the right-coronary sinuses, respectively. The third sinus (the non-coronary sinus) is not visible.

	Patient 1		Patient 2		Patient 3	
	η_s^{MAX}	η_s^{AV}	η_s^{MAX}	η_s^{AV}	η_s^{MAX}	η_s^{AV}
native	1.83	0.89	1.55	0.71	1.75	0.79
stentless	1.70	0.84	1.51	0.69	1.65	0.74
stented	1.49	0.71	1.30	0.59	1.38	0.61

Table 3. Values of η_s^{MAX} and η_s^{AV} at peak systole for all the cases. All the values are given in mm.

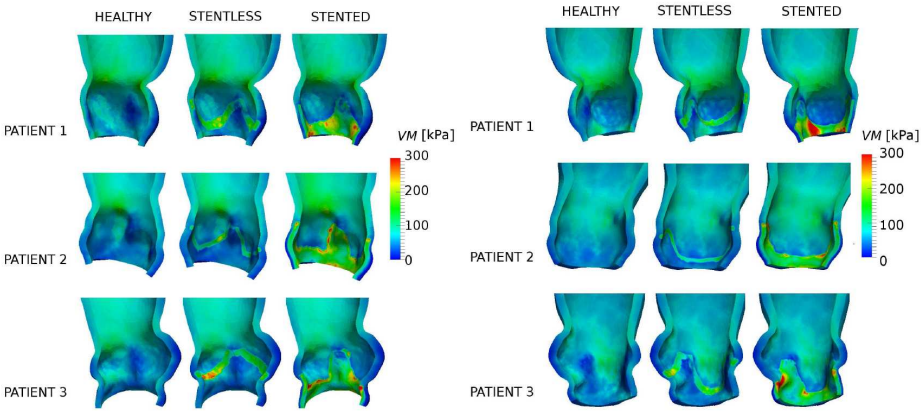

Figure 9. Spatial distribution of the peak systolic Von Mises stresses $VM(t_s, \boldsymbol{x})$ in the anterior (left) and posterior (right) internal wall of the aortic root of Patient 1, Patient 2 and Patient 3, respectively.

3.2.2 Analysis of internal stresses in the aortic root

We characterized the mechanical response of the aortic root by computing the systolic *Von Mises stresses* $VM(t_s, \boldsymbol{x})$ (Leckie and Bello 2009) in the aortic root wall, whose spatial distributions are shown in Figure 9. From these plots, we observe that in the three native cases the Von Mises stresses values were relatively low and uniformly distributed. We also notice that in the stentless configurations these values are closer to the physiological level than in the stented models, where we observe a complex and heterogeneous spatial stress distribution in the region where the polymeric frame was placed.

A more quantitative analysis was performed by computing in the volumes of interest $\mathcal{V}$ the average in space systolic Von Mises stresses, $VM^{AV} = \frac{1}{|\mathcal{V}|}\int_{\mathcal{V}} VM(t_s, \boldsymbol{x})d\boldsymbol{x}$, and the maximum in space systolic Von Mises stresses, $VM^{MAX} = \max_{\boldsymbol{x}\in\mathcal{V}} VM(t_s, \boldsymbol{x})$ (see Table 4). For Patients 1 and 2, we notice that both quantities assumed low values in the native scenarios. The stentless configurations revealed a slight increase in the values of VM^{MAX} , whereas the values of VM^{AV} were not significantly different from those obtained in the native root. In particular, as shown in Figure 9, the highest values of the Von Mises stresses occurred in the region of the suture of the stentless prostheses. On the contrary, the stented scenario showed higher values of VM^{MAX}

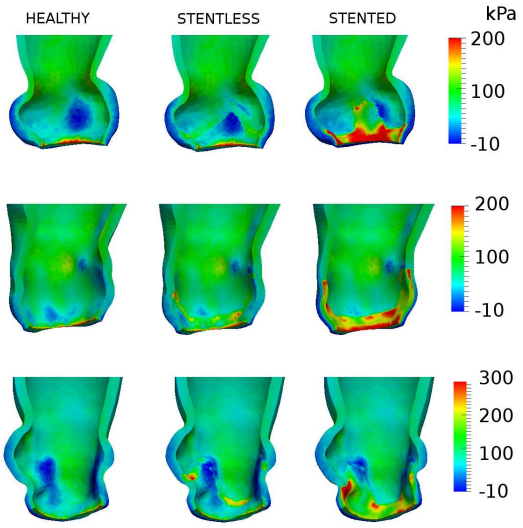

Figure 10. Spatial distribution of the maximum principal stresses in the internal wall of the aortic root of Patient 1, Patient 2 and Patient 3, respectively.

with respect to the native configuration and the value of VM^{MAX} was found in the lower part of the non-coronary sinus in Patient 1 (see Figure 9, right) and between the right-coronary and the left-coronary sinuses in Patient 2 (see Figure 9, left). The stress distribution in Patient 3 showed

	Patient 1		Patient 2		Patient 3	
	VM^{MAX}	VM^{AV}	VM^{MAX}	VM^{AV}	VM^{MAX}	VM^{AV}
native	165	67	169	59	152	56
stentless	202	66	192	56	230	55
stented	367	83	349	64	491	69

Table 4. Values of VM^{MAX} and VM^{AV} at peak systole for all the cases. All the values are given in kPa.

notable differences with respect to the native case in both the stentless and stented configurations. In particular, VM^{MAX} reaches a value 50% higher than the physiological level in the suture region of the stentless prosthesis, and a value 220% higher in the lower part of both the left and the right-coronary sinuses in the stented scenario (see Figure 9).

In view of a more complete analysis, in Figure 10 we reported the *principal normal stresses* representing the eigenvalues of the Cauchy stress tensor, to characterize the presence of both compressed and stretched regions (Grande-Allen, Cochran, et al. 2001; De Hart, Baaijens, et al. 2003). One may note a homogeneous stress distribution in both the stentless and native configurations where compressive stresses were found in the regions comprised between the Valsava sinuses. On the contrary, the stented scenarios revealed a more complex and heterogeneous spatial distributions with high tensile stresses values computed in the region of the rigid frame.

4. Discussion

4.1 *The choice of the computational model*

In the last decades considerable attention has been paid to simulate the effect of the fluid-dynamics entering the ascending aorta on the aortic valve leaflets and/or the aortic root. One of the reasons for such an interest is the need of quantitative structural stress data to support the design of the prostheses commonly adopted in surgical practice.

In the literature different models have been considered so far in the context of both stentless and stented prostheses. Purely mechanical studies were carried out by using both idealized (Cacciola, Peters and Schreurs 2000; Li, Luo and Kuang 2001; Arcidiacono, Corvi and Severi 2005; Xiong, Goetz, et al. 2010) and patient-specific geometries (Auricchio, Conti, et al. 2011, 2014; Morganti, Conti, et al. 2014). These works focused on the structural stresses in the valve leaflets and in the aortic root, but ignored the fluid-dynamics inside the root.

In De Hart, Peters, et al. (2003, 2004) the authors modeled the interaction between the blood fluid-dynamics and the leaflets under the assumption of rigid aortic root walls, to simulate the stented case. They assumed an axi-symmetric hypothesis of the domain and a Reynolds number $Re = 900$ smaller than the physiological one. In De Hart, Baaijens, et al. (2003); Hsu, Kamensky, et al. (2014); Kamensky, Hsu, et al. (2014), the also the interaction between blood and compliant root in the stentless case was accounted for. Again, these works focused on simplified geometries and/or simplified flow assumptions.

Concerning the modeling of the prostheses, the frame of the stented one was either ignored (Arcidiacono, Corvi and Severi 2005) or included in the case of rigid aortic root (Cacciola, Peters and Schreurs 2000; De Hart, Peters, et al. 2003, 2004). The suture line in the stentless case was either ignored (Auricchio, Conti, et al. 2011, 2014; De Hart, Baaijens, et al. 2003), or modeled with the same properties of the leaflets (Xiong, Goetz, et al. 2010), or treated as a rigid material (Hsu, Kamensky, et al. 2014; Kamensky, Hsu, et al. 2014).

In this context, the present work considered an FSI model between the blood and the aortic root, in order to compare the different wall stresses experienced by the aortic wall in the three different scenarios. To perform this comparison, we assumed a different mechanical behavior for the different regions characterizing the prostheses. In particular, for the stented case we stiffened only the area in which the stent frame is actually sewn and not the entire aortic root as commonly done, whereas for the stentless case we considered a stiffening in the sewing ring (see Figure 3). This is an original contribution of the present work, indeed in the previous studies the wall of the aortic root was assumed mechanically uniform.

Another important feature of our model is the use of physiological geometrical and dynamic data to reproduce the three scenarios. This allowed to obtain physiological Reynolds numbers in real geometries reconstructed from CT images, suitably deflated to recover the zero-stress configuration.

4.2 *Mechanical performances of stentless and stented bio-prostheses and clinical implications*

The primary goal of this work is to carry out a comparison of the mechanical performance of stentless and stented bio-prostheses. In what follows, we discuss some issues.

First, the results obtained in the native configuration showed a good agreement with the literature. In particular, in De Paulis, De Matteis, et al. (2001) the root dimensions at the level of the Valsalva sinuses and STJ were quantified by echocardiographic measurements, which revealed displacements of about $0.75\,mm$ (corresponding to a diameter variation of $1.5\,mm$), thus in agreement with our numerical results (see subfigures on the left in Figure 7). Moreover, measurements on sheep revealed a qualitative agreement of the systolic displacements with our results also at the commissures, where greater displacements were observed in (Lansac, Lim, et al. 2002). The Von Mises Stress values were in accordance with the numerical results presented in (Becker, Rowson, et al. 2011), that suggested systolic VM stresses in the range $(140 - 200)\,kPa$.

The second and most relevant issue regards the significant differences observed by comparing the mechanical performances of the stentless and stented bio-pro-stheses, in terms of both displacements and stresses spatial distribution. In particular, the presence of the rigid frame in the stented scenarios caused a reduction of about 20% in the values of η_s^{AV} and η_s^{MAX} with respect to that of the native situation. On the contrary, negligible differences were observed between the stentless and the native configurations. Such a trend was also confirmed by computing the Von Mises Stress stresses and the maximum principal stresses. In this case, very high stress values were found in

all the stented configurations with respect to the corresponding native scenario. Again, negligible differences (especially for Patients 1 and 2) were observed between the stentless and the native scenarios. Consequently, as a first immediate clinical implication of the results here presented, we point out that the stentless bio-prostheses seems to recover a more physiological dynamics.

The third important issue of our study regards the clinical implication related to the placement of the suture of the stentless prosthesis on the aortic root. Indeed, we found elevated Von Mises stresses for Patient 3 in correspondence of the change of curvature at the Valsalva sinuses, where the suture has been placed. Instead, for Patients 1 and 2 where the sewing ring has been placed below the region of curvature changes, we found low stress values, comparable with the native ones. This suggests that the placement of the sewing ring may provide a better recovery of the physiological mechanical behavior.

4.3 *Limitations*

As a first approximation, we decided to neglect the inclusion of the leaflets, so as to simplify the analysis. This was justified, since we were comparing mechanical quantities in the aortic root wall, rather than in the leaflets. Moreover, we were interested in analyzing some quantities at the systole, when the leaflets are completely open. We observed from our results a fully developed jet downstream the aortic orifice, which remained confined to the core region of the aortic root, in agreement with experimental findings for stentless and stented bio-prostheses (Kvitting, Dyverfeldt, et al. 2010; Lim, Chew, et al. 2001). Such an agreement demonstrated that our numerical models were able to capture the main effects of the systolic blood dynamics in the aortic root and for this reason we believe that the mechanism of opening/closing could be ignored as a first approximation for our purposes.

References

Angell WW, Yoon DL. 1977. Heart valve stent and process for preparing a stented heart valve prosthesis. US Patent 4,035,849.

Antiga L, Piccinelli M, Botti L, Ene-Iordache B, Remuzzi A, Steinman DA. 2008. An image-based modeling framework for patient-specific computational hemodynamics. Medical & biological engineering & computing. 46(11):1097–1112.

Arcidiacono G, Corvi A, Severi T. 2005. Functional analysis of bioprosthetic heart valves. Journal of biomechanics. 38(7):1483–1490.

Auricchio F, Conti M, Ferrara A, Morganti S, Reali A. 2014. Patient-specific simulation of a stentless aortic valve implant: the impact of fibres on leaflet performance. Computer methods in biomechanics and biomedical engineering. 17(3):277–285.

Auricchio F, Conti M, Morganti S, Totaro P. 2011. A computational tool to support pre-operative planning of stentless aortic valve implant. Medical engineering & physics. 33(10):1183–1192.

Badia S, Nobile F, Vergara C. 2008. Fluid-structure partitioned procedures based on Robin transmission conditions. Journal of Computational Physics. 227:7027–7051.

Becker W, Rowson J, Oakley J, Yoxall A, Manson G, Worden K. 2011. Bayesian sensitivity analysis of a model of the aortic valve. Journal of biomechanics. 44(8):1499–1506.

Beholz S, Claus B, Dushe S, Konertz W. 2006. Operative technique and early hemodynamic results with the freedom solo valve. Journal of heart valve desease. 15(3):429.

Bernacca GM, OConnor B, Williams DF, Wheatley DJ. 2002. Hydrodynamic function of polyurethane prosthetic heart valves: influences of young's modulus and leaflet thickness. Biomaterials. 23(1):45–50.

Bols J, Degroote J, Trachet B, Verhegghe B, Segers P, Vierendeels J. 2013. A computational method to assess the in vivo stresses and unloaded configuration of patient-specific blood vessels. Journal of Computational and Applied Mathematics. 246:10–17.

Burman E, Hansbo P. 2006. Edge stabilization for the generalized Stokes problem: a continuous interior penalty method. Computer Methods in Applied Mechanics and Engineering. 195:2393–2410.

Cacciola G, Peters G, Schreurs P. 2000. A three-dimensional mechanical analysis of a stentless fibre-reinforced aortic valve prosthesis. Journal of Biomechanics. 33(5):521–530.

De Hart J, Baaijens F, Peters G, Schreurs P. 2003. A computational fluid-structure interaction analysis of a fiber-reinforced stentless aortic valve. Journal of biomechanics. 36(5):699–712.

De Hart J, Peters G, Schreurs P, Baaijens F. 2003. A three-dimensional computational analysis of fluid–structure interaction in the aortic valve. Journal of biomechanics. 36(1):103–112.

De Hart J, Peters G, Schreurs P, Baaijens F. 2004. Collagen fibers reduce stresses and stabilize motion of aortic valve leaflets during systole. Journal of biomechanics. 37(3):303–311.

De Paulis R, De Matteis GM, Nardi P, Scaffa R, Buratta MM, Chiariello L. 2001. Opening and closing characteristics of the aortic valve after valve-sparing procedures using a new aortic root conduit. The Annals of thoracic surgery. 72(2):487–494.

de Putter S, Wolters B, Rutten M, Breeuwer M, Gerritsen F, van de Vosse F. 2007. Patient-specific initial wall stress in abdominal aortic aneurysms with a backward incremental method. Journal of Biomechanics. 40:10811090.

Demiray H. 1972. A note on the elasticity of soft biological tissues. Journal of biomechanics. 5(3):309–311.

Dunning J, Graham R, Thambyrajah J, Stewart M, Kendall S, Hunter S. 2007. Stentless vs. stented aortic valve bioprostheses: a prospective randomized controlled trial. European heart journal. 28(19):2369–2374.

Faggiano E, Antiga L. in preparation. An open-source tool for patient-specific fluid-structure vessel mesh generation.

García-Herrera CM, Celentano DJ. 2013. Modelling and numerical simulation of the human aortic arch under in vivo conditions. Biomechanics and modeling in mechanobiology. 12(6):1143–1154.

Gee M, Reeps C, Eckstein H, Wall W. 2009. Prestressing in finite deformation abdominal aortic aneurysm simulation. Journal of Biomechanics. 42:1732–1739.

Grande-Allen KJ, Cochran RP, Reinhall PG, Kunzelman KS. 2001. Finite-element analysis of aortic valve-sparing: influence of graft shape and stiffness. Biomedical Engineering, IEEE Transactions on. 48(6):647–659.

Holzapfel G, Ogden R. 2010. Constitutive modelling of arteries. Proc R Soc Lond Ser A Math Phys Eng Sci. 466(2118):1551–1596. Available from: http://dx.doi.org/10.1098/rspa.2010.0058.

Horgan C, Saccomandi G. 2003. A description of arterial wall mechanics using limiting chain extensibility constitutive models. Biomechanics and modeling in mechanobiology. 1(4):251–266.

Hsu MC, Bazilevs Y. 2011. Blood vessel tissue prestress modeling for vascular fluidstructure interaction simulation. Finite Elements in Analysis and Design. 47:593599.

Hsu MC, Kamensky D, Bazilevs Y, Sacks MS, Hughes TJ. 2014. Fluid–structure interaction analysis of bioprosthetic heart valves: significance of arterial wall deformation. Computational Mechanics. 54(4):1055–1071.

Hughes TJR, Liu WK, Zimmermann TK. 1981. Lagrangian-Eulerian finite element formulation for incompressible viscous flows. Computer Methods in Applied Mechanics and Engineering. 29(3):329–349.

Kamensky D, Hsu Mc, Schillinger D, Evans JA, Aggarwal A, Sacks MS, Hughes TJR, Kamensky RD. 2014. A variational immersed boundary framework for fluid structure interaction : Isogeometric implementation and application to bioprosthetic heart valves. ICES REPORT 14-12. (May).

Koch T, Reddy B, Zilla P, Franz T. 2010. Aortic valve leaflet mechanical properties facilitate diastolic valve function. Computer methods in biomechanics and biomedical engineering. 13(2):225–234.

Kvitting JPE, Dyverfeldt P, Sigfridsson A, Franzén S, Wigström L, Bolger AF, Ebbers T. 2010. In vitro assessment of flow patterns and turbulence intensity in prosthetic heart valves using generalized phase-contrast mri. Journal of Magnetic Resonance Imaging. 31(5):1075–1080.

Lancellotti RM. 2012. Numerical computations of deflated vascular geometries fo fluid-structure interaction in haemodynamics [dissertation]. Universit degli Studi di Napoli Federico II.

Lansac E, Lim H, Shomura Y, Lim K, Rice N, Goetz W, Acar C, Duran C. 2002. A four-dimensional study of the aortic root dynamics. European journal of cardio-thoracic surgery. 22(4):497–503.

Leckie F, Bello D. 2009. Strength and stiffness of engineering systems. Springer.

Li J, Luo X, Kuang Z. 2001. A nonlinear anisotropic model for porcine aortic heart valves. Journal of biomechanics. 34(10):1279–1289.

Lim W, Chew Y, Chew T, Low H. 2001. Pulsatile flow studies of a porcine bioprosthetic aortic valve in vitro: Piv measurements and shear-induced blood damage. Journal of biomechanics. 34(11):1417–1427.

Lloyd-Jones D, Adams RJ, Brown TM, Carnethon M, Dai S, De Simone G, Ferguson TB, Ford E, Furie K, Gillespie C, et al. 2010. Heart disease and stroke statistics2010 update a report from the american heart

association. Circulation. 121(7):e46–e215.

Lu J, Zhou X, Raghavan M. 2007. Inverse elastostatic stress analysis in pre-deformed biological structures: demonstration using abdominal aortic aneurysms. Journal of Biomechanics. 40:693696.

Mackay T, Wheatley D, Bernacca G, Fisher A, Hindle C. 1996. New polyurethane heart valve prosthesis: design, manufacture and evaluation. Biomaterials. 17(19):1857–1863.

Moireau P, Xiao N, Astorino M, Figueroa CA, Chapelle D, Taylor CA, Gerbeau JF. 2012. External tissue support and fluidstructure simulation in blood flows. Biomechanics and Modeling in Mechanobiology. 11(1-2):1–18.

Morganti S, Conti M, Aiello M, Valentini A, Mazzola A, Reali A, Auricchio F. 2014. Simulation of transcatheter aortic valve implantation through patient-specific finite element analysis: Two clinical cases. Journal of biomechanics. 47(11):2547–2555.

Nobile F, Pozzoli M, Vergara C. 2013. Time accurate partitioned algorithms for the solution of fluid–structure interaction problems in haemodynamics. Computers & Fluids. 86:470–482.

Nobile F, Pozzoli M, Vergara C. 2014. Inexact accurate partitioned algorithms for fluid-structure interaction problems with finite elasticity in haemodynamics. Journal of Computational Physics. 273:598–617.

Nordmeyer S, Riesenkampff E, Messroghli D, Kropf S, Nordmeyer J, Berger F, Kuehne T. 2013. Four-dimensional velocity-encoded magnetic resonance imaging improves blood flow quantification in patients with complex accelerated flow. Journal of Magnetic Resonance Imaging. 37(1):208–216.

Olufsen MS, Peskin CS, Kim WY, Pedersen EM, Nadim A, Larsen J. 2000. Numerical simulation and experimental validation of blood flow in arteries with structured-tree outflow conditions. Annals of biomedical engineering. 28(11):1281–1299.

Smuts A, Blaine D, Scheffer C, Weich H, Doubell A, Dellimore K. 2011. Application of finite element analysis to the design of tissue leaflets for a percutaneous aortic valve. J Mech Behav Biomed Materials. 4(1):85–98.

Summers RM, Andrasko-Bourgeois J, Feuerstein IM, Hill SC, Jones EC, Busse MK, Wise B, Bove KE, Rishforth BA, Tucker E, et al. 1998. Evaluation of the aortic root by mri insights from patients with homozygous familial hypercholesterolemia. Circulation. 98(6):509–518.

Wheatley DJ, Fisher J, Williams D. 2001. Heart valve prosthesis. US Patent 6,171,335.

Xiong FL, Goetz WA, Chong CK, Chua YL, Pfeifer S, Wintermantel E, Yeo JH. 2010. Finite element investigation of stentless pericardial aortic valves: relevance of leaflet geometry. Annals of biomedical engineering. 38(5):1908–1918.

Recent publications:

MATHEMATICS INSTITUTE OF COMPUTATIONAL SCIENCE AND ENGINEERING
Section of Mathematics

Ecole Polytechnique Fédérale (EPFL)

CH-1015 Lausanne

31.2015 ANNA TAGLIABUE, LUCA DEDÈ, ALFIO QUARTERONI:
Fluid dynamics of an idealized left ventricle: the extended Nitsche's method for the treatment of heart valves as mixed time varying boundary conditions

32.2015 ASSYR ABDULLE, ONDREJ BUDÁČ:
A discontinuous Galerkin reduced basis numerical homogenization method for fluid flow in porous media

33.2015 ASSYR ABDULLE:
Numerical homogenization methods for parabolic monotone problems

34.2015 JÖRG LIESEN, ROBERT LUCE:
Fast recovery and approximation of hidden Cauchy structure

35.2015 ASSYR ABDULLE, MARTIN HUBER:
Numerical homogenization method for parabolic advection-diffusion multiscale problems with large compressible flows

36.2015 ASSYR ABDULLE, ORANE JECKER, ALEXANDER SHAPEEV:
An optimization based coupling method for multiscale problems

***

01.2016 ANDREA MANZONI, FEDERICO NEGRI, ALFIO QUARTERONI:
Dimensionality reduction of parameter-dependent problems through proper orthogonal decomposition

02.2016 SHENFENG ZHU, LUCA DEDÈ, ALFIO QUARTERONI:
Isogeometric analysis and proper orthogonal decomposition for the acoustic wave equation

03.2016 ROBERT LUCE, PETER HILDEBRANDT, UWE KUHLMANN, JÖRG LIESEN,:
Using separable non-negative matrix factorization techniques for the analysis of time-resolved Raman spectra

04.2015 ASSYR ABDULLE, TIMOTHÉE POUCHON:
Effective models for the multidimensional wave equation in heterogeneous media over long time and numerical homogenization

05.2016 ALFIO QUARTERONI, TONI LASSILA, SIMONE ROSSI, RICARDO RUIZ-BAIER:
Integrated heart – Coupling multiscale and multiphysics models for the simulation of the cardiac function

06.2016 M.G.C. NESTOLA, E. FAGGIANO, C. VERGARA, R.M. LANCELLOTTI, S. IPPOLITO, S. FILIPPI, A. QUARTERONI, R. SCROFANI :
Computational comparison of aortic root stresses in presence of stentless and stented aortic valve bio-prostheses